



Lagrangian analysis of sweeping jets measured by time-resolved particle image velocimetry

Xin Wen, Yingzheng Liu*

Key Lab of Education Ministry for Power Machinery and Engineering, School of Mechanical Engineering, Shanghai Jiao Tong University, 800 Dongchuan Road, Shanghai 200240, China

Gas Turbine Research Institute, Shanghai Jiao Tong University, 800 Dongchuan Road, Shanghai 200240, China

ARTICLE INFO

Keywords:

Sweeping jet
Deformation of jet column
Lagrangian transformation
TR-PIV
DMD

ABSTRACT

The flow dynamics of a sweeping jet generated by a fluidic oscillator is experimentally investigated by time-resolved particle image velocimetry (TR-PIV). Lagrangian transformation is applied to the measured flow fields to better determine the characteristics of the jet flow outside the oscillator. Upon increasing the Reynolds number from $Re = 2.5 \times 10^3$ to 11.7×10^3 , which respectively corresponds to the occurrences of straight and deflected jet columns, the spreading angle of the external jet increases and reaches its saturation value. The overall performance of the flow fields is first examined in Eulerian space. At the higher Reynolds number, the momentum is more directed at the maximum deflected positions of the jet. A clear weak flow is then induced at the middle of the far field region from the jet nozzle. The induced jet column is also bent significantly into a curved shape. To examine the variations of the jet flows with different column shapes, Lagrangian transformation is applied to the measured flow fields by attaching a rotating reference frame on the jet column. It is found that the large bending angle of the jet column at the higher Reynolds number induces higher fluctuations and more uneven oscillation patterns in the jet flow. In the far field region at the higher Reynolds number, the time-averaged jet velocity decreases faster, with higher turbulence intensities than those at the lower Reynolds number. The phase-dependent jet flow fields confirm that the peak velocity and the jet width also have higher fluctuations at the higher Reynolds number. In addition, the jet bending angle in the far field region shows more uneven oscillation patterns compared with those in the near field region. These highly fluctuating and uneven flow behaviors contribute to the uneven distribution of the jet momentum at the higher Reynolds number in Eulerian space. Finally, different fluctuating behaviors of the jet flow due to the different jet shapes are also revealed by Lagrangian dynamic mode decomposition (DMD).

1. Introduction

The sweeping jet, which relies on the intrinsic flow instability of a fluidic oscillator without moving parts, has shown ever-increasing potential in flow control applications, including separation control [12,5] and heat transfer enhancement [1,5]. In such configurations, it is well established that the control strategy and its effectiveness are closely related to the highly unsteady spatio-temporal behaviors of the sweeping jet flow. However, in marked contrast to a straight steady jet, the sweeping jet strongly oscillates in the transverse direction coupled with the instantaneously varying flow behaviors of the deflected jet during oscillation [17], introducing considerable complication into the unsteady flow dynamics. Accordingly, it is highly desirable to quantify the characteristics of the unsteady events superimposed in the sweeping

jet flow.

Despite demonstrations that the fluidic oscillator can provide efficient flow control, very few efforts have been made to determine the unsteady characteristics of the sweeping jet flow. By applying the fluidic oscillator in flow separation control, Koklu [5] found that a larger spreading angle of the emitted sweeping jet would generate a larger jet-influenced area. Ostermann [7] showed that a larger spreading angle yielded an uneven spatial distribution of jet momentum in the time-averaged flow field, whereas a smaller spreading angle yielded an even distribution. To examine the oscillation patterns of the sweeping jet in the near field region of the jet nozzle ($x < 3d_h$), the unsteady flow field measured by particle image velocimetry (PIV) was transformed from Cartesian to polar coordinates [4]. The phase-dependent jet deflection angles indicated that when the jet had a large

* Corresponding author at: Key Lab of Education Ministry for Power Machinery and Engineering, School of Mechanical Engineering, Shanghai Jiao Tong University, 800 Dongchuan Road, Shanghai 200240, China.

E-mail address: yzliu@sjtu.edu.cn (Y. Liu).

<https://doi.org/10.1016/j.exptthermflusci.2018.04.014>

Received 26 March 2018; Received in revised form 15 April 2018; Accepted 16 April 2018
Available online 22 April 2018

0894-1777/ © 2018 Elsevier Inc. All rights reserved.

spreading angle, it dwelled in its deflected state for a long time, before briefly moving over to the opposite side. Using the same method, Wozidlo et al. [17] quantified the substantially fluctuating jet properties (flow rate, jet width and peak velocity) during one oscillation cycle in the near field region. Our previous time-resolved PIV (TR-PIV) study [15] revealed that the jet column was bent into a significantly curved shape when the jet had a large spreading angle, giving rise to an uneven impingement effect on the far field surface. Detailed quantification of the jet flow, especially in the far field region ($x > 3d_h$), is hindered by the strong oscillation of the instantaneous jet column in the transverse direction, but can be achieved using a Lagrangian reference frame traveling with the oscillating jet column. Such a Lagrangian transformation was successfully used to minimize the influence of a flow structure’s motion to allow a focus on its structural variation [13,14].

The major concern of the present study is the spatio-temporally varying behavior of the sweeping jet flow with different column shapes. To this end, Lagrangian transformation is applied to the flow fields. A planar TR-PIV measurement of the sweeping-jet flow fields at six Reynolds numbers (from $Re = 2.5 \times 10^3$ to 11.7×10^3) is performed in a water tank, yielding a wealth of information on the external fluidic oscillator and the region beyond. Particular attention is paid to the external jet flow behaviors at two Reynolds numbers, $Re = 2.5 \times 10^3$ and 11.7×10^3 , which respectively correspond to the occurrences of straight and deflected jet column shapes. The flow fields are first examined in Eulerian space in terms of the overall distribution of velocity and turbulence with fluctuating flow patterns, as extracted by dynamic mode decomposition (DMD). Then, the variations of the sweeping jet flow are analyzed in Lagrangian space. The jet flows with different bent column shapes are examined in terms of the time-averaged velocity, turbulence intensity and phase-dependent jet properties (the jet bending angle, peak velocity and jet width) in the far field. Finally, the fluctuating behaviors of the jet flow are examined by Lagrangian DMD.

2. Methods

2.1. Test platform

The geometry of the fluidic oscillator, shown in Fig. 1, is similar to that used in our previous study [15], but with doubled size. The jet throat has a square cross section with a height (h) of 10 mm, resulting in a hydraulic diameter (d_h) of 10 mm. The depth of the oscillator is 10 mm, and the nozzle has a diverging angle (φ) of 90° and a length of 40 mm at the exit. The experiments are performed in a water tank as shown in Fig. 1. The fluidic oscillator is placed at the center of the tank.

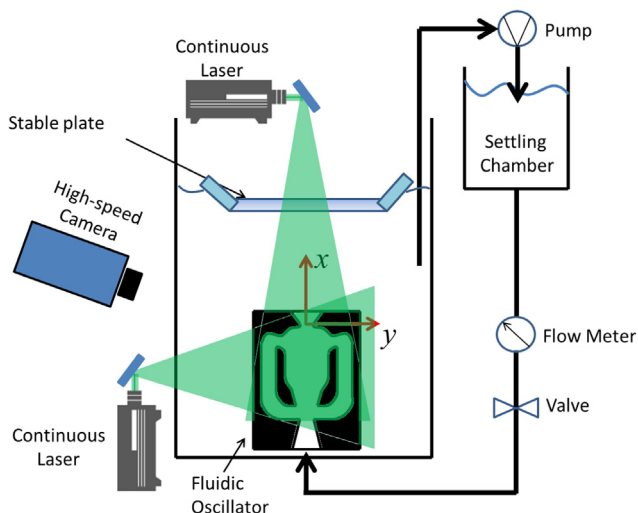
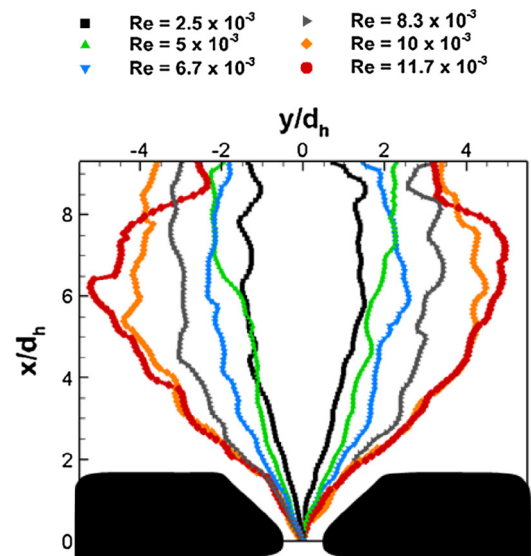
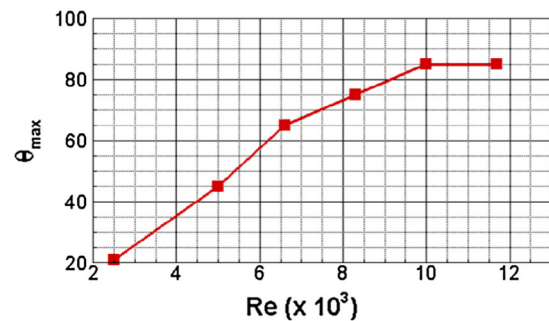


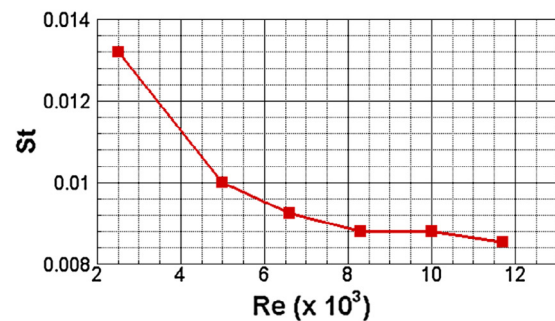
Fig. 1. Sketch of experimental setup (not to scale).



(a) The jet’s maximum deflected positions at six Reynolds numbers



(b) The jet’s maximum spreading angle



(c) Jet oscillation frequency

Fig. 2. (a) The jet’s maximum deflected positions at six Reynolds numbers. (b) The jet’s maximum spreading angle. (c) Jet oscillation frequency. (a) Shapes of the external jet columns at the phase of jet’s maximum deflected positions, (b) The jet’s maximum spreading angle θ_{max} (the uncertainty is about 3° based on the spatial resolution of the PIV measurement) and (c) St versus Reynolds number.

The distance between the oscillator and the side walls of the tank is at least $50d_h$ to prevent influence from the sides. Because a laser sheet is fired from top to bottom through the stable plate, a rim is added to obstruct the water in order to avoid an unstable liquid interface. The distance from jet nozzle to the stable plate is fixed at about $30d_h$ to avoid the adverse pressure gradient in the area of interest. Water is channeled from an overhead settling chamber and driven by gravity into the oscillator. A flowmeter monitors and controls the volume flow rate of the jet with an uncertainty level of 2.5%. By tuning the

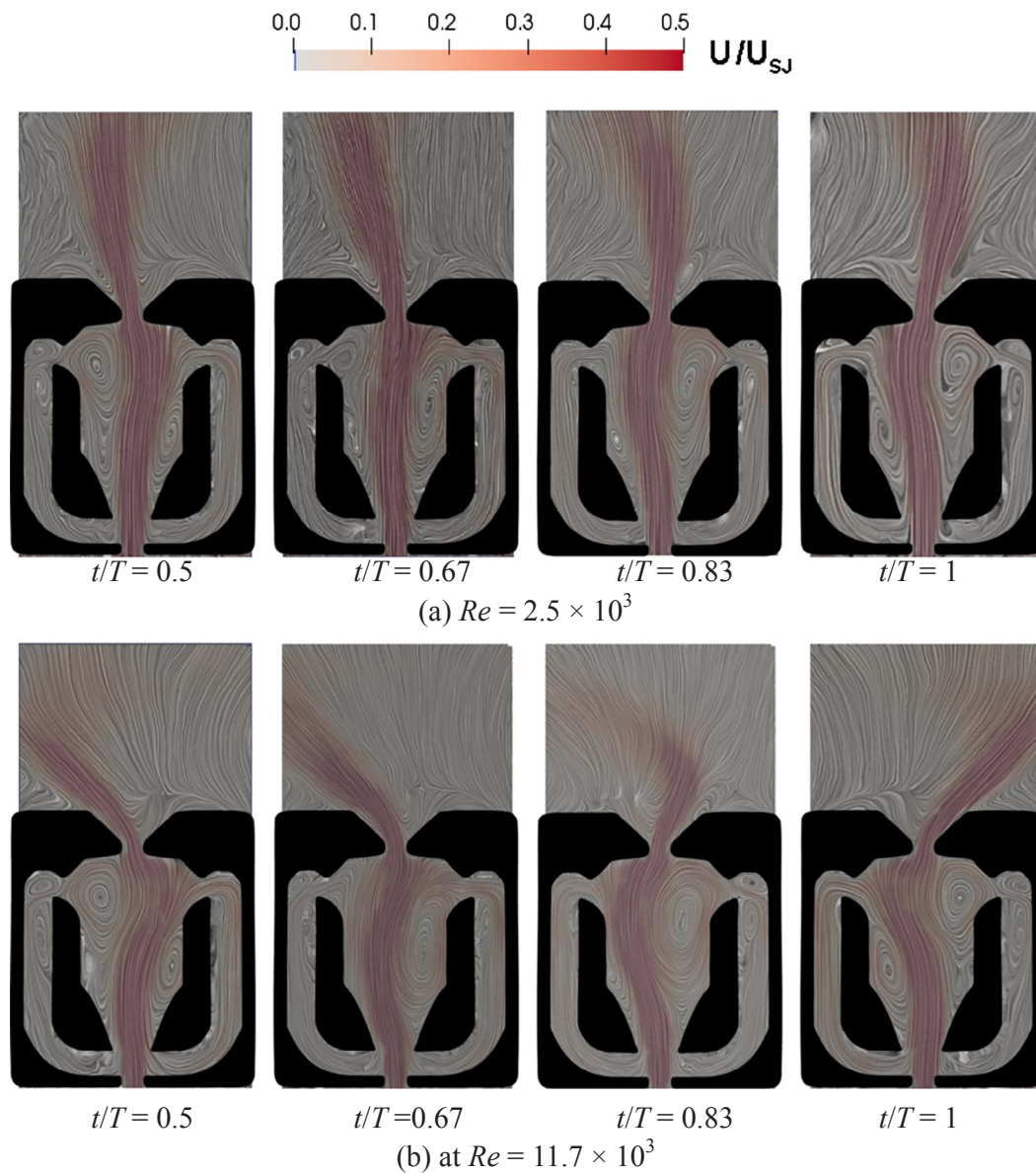


Fig. 3. Time sequences of phase-averaged flow fields both inside and outside of the oscillator with streamlines and contour of velocity magnitude.

flowmeter, six Reynolds numbers based on the jet velocity U_{Sj} and hydraulic diameter are obtained, ranging from 2.5×10^3 to 11.7×10^3 , within which the starting process of the jet oscillation is captured. The origin of the Eulerian coordinate system is set at the center of the jet nozzle, with the x-axis pointing in the jet's axial direction and the y-axis pointing in the transverse direction (i.e. the direction of the jet's sweeping motion).

2.2. TR-PIV measurement

TR-PIV is used to measure the highly unsteady flow fields. To obtain good illumination inside the oscillator, two continuous lasers fire simultaneously from two directions. As shown in Fig. 1, two 5-W, 532-nm-wavelength diode-pumped solid-state continuous-wave lasers provide two laser sheets approximately 1 mm thick. To facilitate the PIV measurements, the entire water tunnel is seeded with glass beads ($\rho \approx 1050 \text{ kg/m}^3$, $d \approx 10 \mu\text{m}$) as tracer particles. A high-speed camera (dimax HS4, pco.) operates at a dynamic sampling rate ranging from 0.6 kHz to 2 kHz depending on the Reynolds number. A multigrid cross-correlation technique [9], in combination with subpixel recognition by

Gaussian fitting [18], is applied with a final interrogation window size of 16×16 pixels with 50% overlap. In this time-resolved measurement, a measurement grid of velocity vectors with a spacing of about $1.0 \times 1.0 \text{ mm}$ is then obtained. Due to the strong velocity gradient on the jet's shear layer, more tracking particles are added to the settling chamber to ensure at least 8 particles per interrogation window. As the major source of uncertainty, the root-mean-square fluctuation of the PIV-measured particle displacement is estimated to be about 0.08 pixel in the field images [16]. Therefore, the uncertainties in the measurements determined by recursive image interrogation are approximately 2% in the axial and transverse direction velocity components when the particle displacement is about 4 pixels in the interrogation window. To accelerate the computation, the correlation scheme on the raw seeding pictures is designed as 1-2, 3-4, 5-6, etc. The sampling frequency of the flow vector field is at least two orders of magnitude higher than the examined oscillation frequency of the sweeping jets, which is adequate to resolve the major frequencies in the unsteady flow fields. The total recording time is also dynamic to ensure at least 50 cycle periods are captured for each case. Despite using two lasers, there are still some small dark regions inside the oscillator due to its complex geometry.

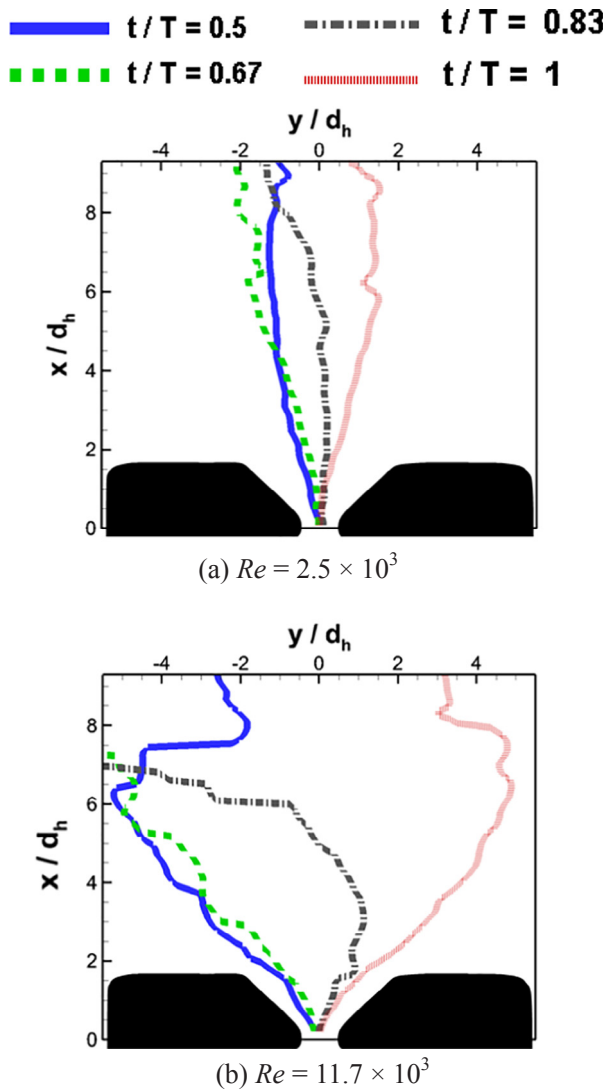


Fig. 4. Shapes of the external jet columns during one half sweeping cycle (the jet switches from left to right side in the near field region).

Hence, the positions of the laser sources are altered twice to fill in the dark regions. The resulting flow fields are phase-averaged, phase-aligned and merged.

3. Data analysis

3.1. Phase-averaging method

A phase indicator is needed to reveal the phase-dependent variation of the sweeping impingement jet. In our previous study [15], phases were identified using the time-resolved velocity signal in the external region. In this study, the sampling rate of the TR-PIV measurement is at least two orders of magnitude higher than the oscillation frequency of the sweeping jet, which provides adequate temporal resolution for phase identification. Therefore, the velocity information extracted from individual PIV snapshots is used for phase identification. Two specific locations in the flow field are selected to yield time-resolved values of the difference between the transverse velocities (along the y -direction). These locations are in the near-exit region and are symmetrical about the center line of the jet nozzle to yield a signal (i.e. time-resolved values of velocity difference) with a high signal-to-noise ratio. Following the procedures used by Ostermann et al. [8] and Woszidlo et al. [17], a numerical low-pass filter is imposed on the signal to reduce the

noise while retaining its phase and amplitude information. The entire signal is then correlated with a segment of the same signal to yield the correlation coefficient. Details of the phase identification can be found in previous studies [8,17,15]. The size of the phase angle window for averaging is 3° in this study, a choice that sufficiently reduces noise while retaining the detailed flow features. As such, more than 150 instantaneous flow fields are used for phase averaging. The time frame used in this study is therefore defined according to external flow. The cycle begins when the jet in the near field region of the jet nozzle is at the deflection position furthest to the right, that is, $t/T = 0$. When the jet switches to the deflection position furthest to the left, $\beta/\pi = 0.5$. The oscillation frequency is also calculated based on the differential velocity signal from the two reference positions.

3.2. DMD analysis

The DMD method decomposes a flow field into its mean value and higher fluctuating modes. As it extracts spatial modes based on frequency content, DMD is suitable for analyzing the dynamics of a flow system involving multiple frequency components. The detailed fundamentals and mathematical processes of the DMD algorithm were provided by Schmid [10,11]. In our previous study [15], DMD was used to extract the major fluctuating patterns in the flow field of a sweeping jet. The mathematical description of DMD is only briefly introduced here.

In DMD, the data are represented in the form of a snapshot sequence, as a matrix

$$U_1^N = \{\mathbf{u}_1, \mathbf{u}_2, \dots, \mathbf{u}_N\} \quad (1)$$

where \mathbf{u}_i stands for a snapshot of the flow field at time t_i and N is the total number of flow fields. In the first step, we assume that a linear mapping A connects the flow fields U_1^N and U_2^{N+1} . The coefficients of the linear combination are stacked in a companion matrix C such that:

$$U_2^{N+1} = AU_1^N \approx U_1^N C \quad (2)$$

where the eigenvalues λ_i of C are approximations to some of the eigenvalues of a higher-dimension inter-snapshot linear map A . QR-decomposition of the data sequence U_1^N is used to calculate the companion matrix C . After the decomposition, we have the following expression for the dynamic modes:

$$\Phi_i = U_1^N v_i \quad (3)$$

where $\Phi_n(x)$ is the spatial basis-mode function and v_i is the i th eigenvector of C . The frequency of Φ_i is then defined as $f = \text{Im}\{\log(\lambda_i)\}/2\pi\Delta t$.

In this study, the instantaneous flow field snapshots are taken at least once every 50 sweeping cycles. Due to the computational limit of the workstation, the sampling frequency of the flow field snapshot is reduced to 75 Hz and 250 Hz for the cases of $Re = 2.5 \times 10^3$ and 11.7×10^3 , respectively. These sampling frequencies are still two orders larger than the sweeping frequencies at these two Reynolds numbers, respectively. DMD is applied in both Eulerian and Lagrangian spaces. Previous studies revealed that Lagrangian DMD can represent a moving structure using fewer modes than the traditional DMD in Eulerian space [13,14]. The underlying mechanism is to impose a moving frame on the structure. In this study, Lagrangian transformation and corresponding DMD analysis are applied to explore the variation of the sweeping jet flow.

4. Results

Fig. 2 shows the overall performance of the oscillator, and Fig. 2a presents the bilateral maximum positions of the jet column at the six Reynolds numbers. The shape of the jet column is described with respect to its center, which is defined by the location of maximum velocity. Similar to our previous findings [15], the jet spreading angle increases with Reynolds number until it reaches its saturation value at $Re = 10 \times 10^3$ due to the constraint of the oscillator geometry. As

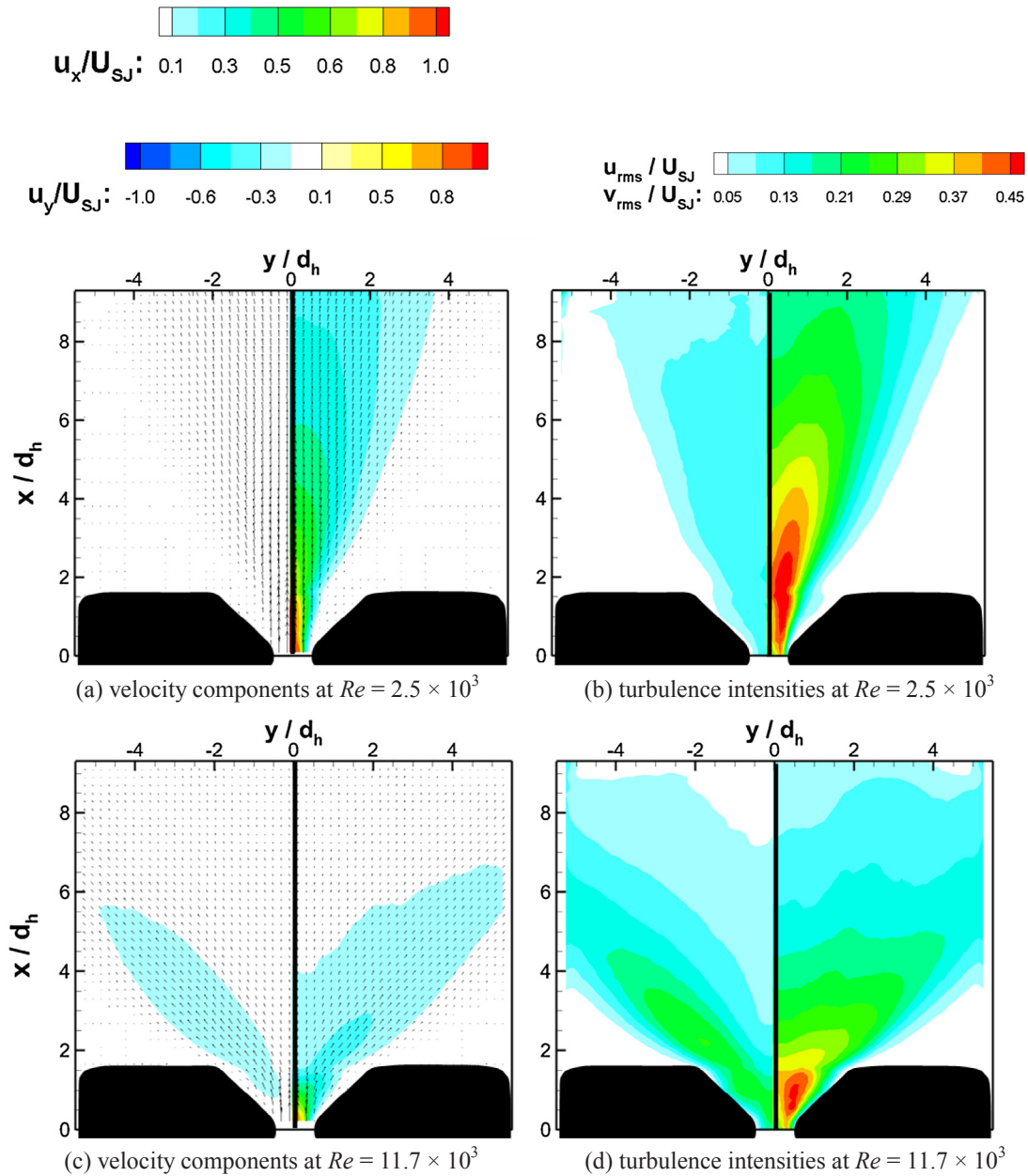


Fig. 5. Time-averaged streamwise velocity along x-direction (right part of the figure) and transverse velocity along y-direction (left side of the figure), and turbulence intensities in streamwise direction (right part of the figure) and transverse direction (left side of the figure), at $Re = 2.5 \times 10^3$ and $Re = 11.7 \times 10^3$. (a) Velocity components at $Re = 2.5 \times 10^3$. (b) Turbulence intensities at $Re = 2.5 \times 10^3$. (c) Velocity components at $Re = 11.7 \times 10^3$. (d) turbulence intensities at $Re = 11.7 \times 10^3$.

shown in Fig. 2b, the jet spreading angle increases from $\theta_{max} \approx 20^\circ$ at $Re = 2.5 \times 10^3$ to a saturation value of $\theta_{max} \approx 85^\circ$ at $Re = 10 \times 10^3$. Therefore, in addition to saturation, this study also captures the starting process of the jet oscillation, during which the oscillation frequency behaves differently than in the saturation stage. Fig. 2c plots the variation with Reynolds number of the Strouhal number St , which is defined as

$$St = \frac{fd_h}{U_{SJ}} \quad (4)$$

where f is the oscillation frequency. The frequency is measured along a horizontal line at $x = 2.5d_h$. The measurement point is located at the maximum deflected position of the jet. Previous studies have found that St is almost independent of the Reynolds number in the saturation stage [17]. In this study, St decreases with the Reynolds number to a constant

value during the starting process of the jet oscillation. From the definition, the constant St means that the oscillating frequency increases linearly with the jet velocity (or Reynolds number), as a result of the short wave length.

To investigate the reasons for the different external flow performances, the flow dynamics inside the oscillator was plotted (Fig. 3). Previous studies have found that the oscillation mechanism is based on separation bubbles between the jet and the mixing chamber walls inside the oscillator, which push the jet to oscillate [2,17]. Herein, the size of the separation bubbles increases with the Reynolds number. To show the internal flow dynamics, the time sequences of the phase-averaged flow fields at two Reynolds numbers, i.e. $Re = 2.5 \times 10^3$ and $Re = 11.7 \times 10^3$, are presented and compared in Fig. 3a and 3b, respectively. One half oscillation cycle is presented, during which the external jet switches from the left-most position to the right-most

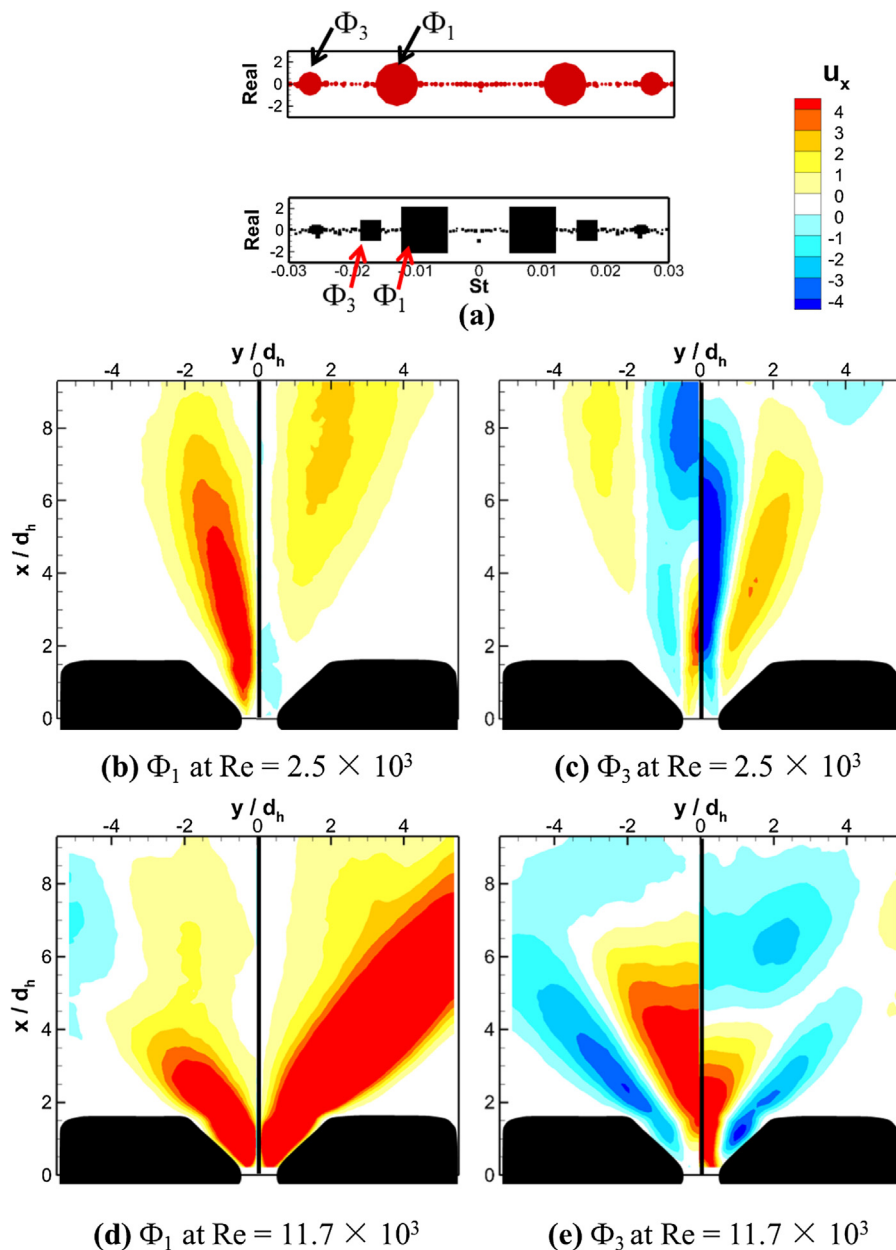


Fig. 6. (a) Energy and frequency spectra of DMD modes (size of the solid symbols indicates the captured energy of each mode), (b-e) contour of streamwise velocity captured by the first two mode-pairs (real part on the left of the figure and imaginary part on the right), at $Re = 2.5 \times 10^3$ and $Re = 11.7 \times 10^3$.

position, i.e. $0.5 \leq t/T \leq 1$. To enhance the visualization, line integral convolution (LIC) [3] is applied to add streamlines over the contour of velocity magnitude. At both Reynolds numbers, the internal flow dynamics are generally similar. Two separation bubbles are found between the main jet and the side walls of the mixing chamber at $t/T = 0.5$. During the oscillation period, one bubble increases in size, whereas the other decreases. Therefore, the bilateral competition between the separation bubbles drives the oscillation of the main jet. At the higher Reynolds number, the separation bubbles are clearly larger. Therefore, the main jet is more strongly deflected inside the mixing chamber, resulting in a larger spreading angle of the external jet. Woszidlo et al. [17] found that the oscillation frequency mainly depended on the growth time of the separation bubble. They also proposed that the oscillation frequency may be decreased by enlarging the total required volume of the separation bubble, which is confirmed by the current results.

4.1. External flow dynamics in Eulerian space

The phase-dependent emitted jet flow and overall performances of the external flow fields are very different at the two selected Reynolds numbers, i.e. $Re = 2.5 \times 10^3$ and 11.7×10^3 . Fig. 4a and 4b show the variation of the external jet column shape at four equally distributed phases during one half oscillation cycle, $0.5 \leq t/T \leq 1$, in the two cases. At the lower Reynolds number, the jet column maintains an almost straight shape during the oscillation, with a small bending angle. However, at the higher Reynolds number, the jet column has a much larger bending angle in the far field region from the jet nozzle. In addition, the jet column shape also changes significantly between phases during the oscillation cycle. For example, the jet column is almost straight at $t/T = 0.67$, but highly bent at $t/T = 0.83$.

Due to the phase dependence of the jet flows, the overall performances of the external flow fields are also very different at the two Reynolds numbers. Fig. 5 presents the time-averaged velocity

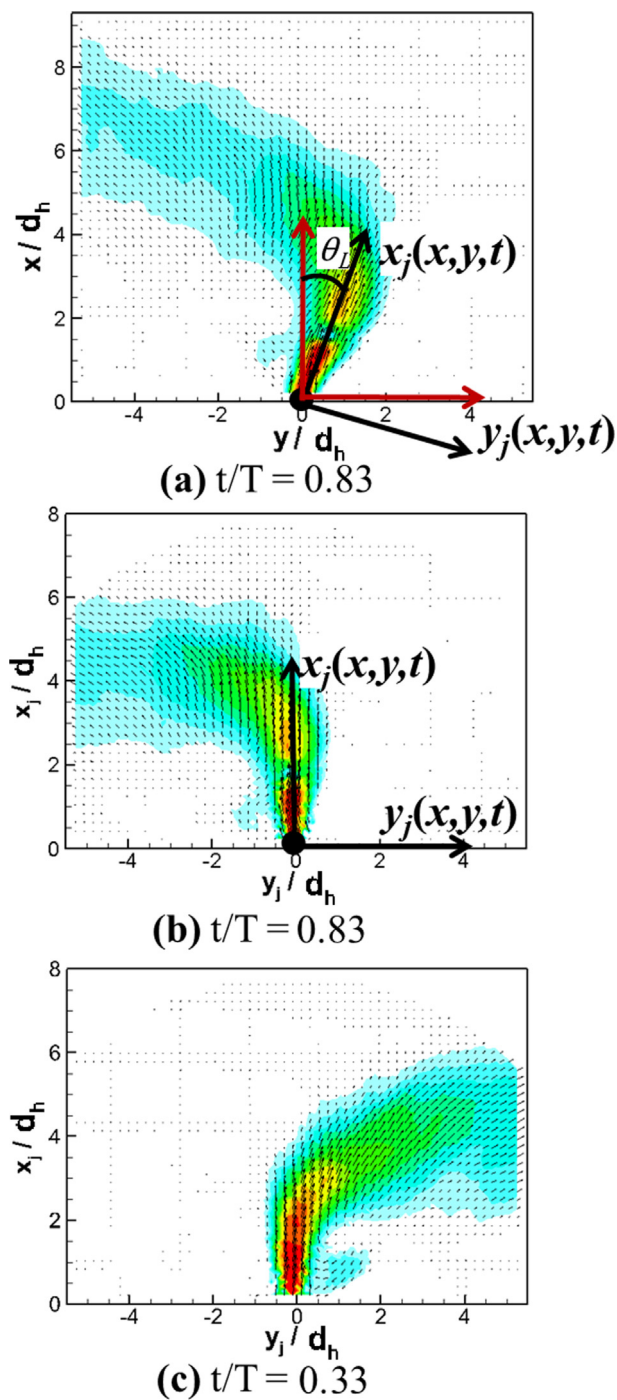


Fig. 7. Transformation of a phase-averaged external flow field from Eulerian (a) to Lagrangian (b) space. Flow fields at (b) and (c) are at the two phases in Lagrangian space where the jet column in the far field has the largest bending angle.

components and turbulence intensities in the flow fields. The time-averaged flow field at the lower Reynolds number resembles a continuous steady jet due to the small spreading angle. As shown in Fig. 5a the majority of the jet momentum is directed in the streamwise direction along the x-axis on the right side of the figure, leaving very weak spanwise jet momentum along the y-axis on the left side. In the near field of the jet nozzle, the streamwise velocity is close to the jet velocity U_{Sj} at the central portion of the jet. As the jet develops to the far field region, the streamwise velocity decreases rapidly due to the enlarged jet-influenced area. The distribution of turbulence intensities is

generally similar to that of velocity components, as shown in Fig. 5b. The story is very different at the higher Reynolds number. As shown in Fig. 5c, the jet momentum is more strongly directed from the streamwise to the transverse direction because of the jet spreading angle of about $\pm 45^\circ$. In addition, similar to our previous findings [15], the distribution of jet momentum is highly uneven. The jet momentum is heavily directed toward both bilateral sides. This bilateral bias is particularly pronounced in the far field from the jet nozzle, leaving a very weak flow in the middle region. The distribution of turbulence components changes accordingly.

In addition to the time-averaged flow fields, the major fluctuating flow patterns are also uneven at the higher Reynolds number, as analyzed by DMD. Fig. 6a presents the energy and frequency spectra of the fluctuating DMD modes. The energies of the DMD modes were normalized by the energy of the zero DMD mode, which corresponds to the time-averaged flow field. The resulting fluctuating modes are coupled into pairs. Each symbol corresponds to a single DMD mode, and its size is proportional to the mode energy. The energy and frequency spectra at the two Reynolds numbers are generally similar. The first mode-pair $[\Phi_1, \Phi_2]$ has almost double the energy of the second $[\Phi_3, \Phi_4]$. The frequency of the first mode-pair is the oscillation frequency, while that of the second is double this frequency. Within each pair, the real parts of the two modes are same, whereas the imaginary parts are opposite. Therefore, each mode-pair can be represented using only one mode. As shown in Fig. 6b and d, at the two Reynolds numbers, the first mode-pair mostly captures the flow patterns at the bilateral sides of the flow field. As shown in Fig. 6c and e, the second mode-pair mostly captures the flow patterns around the center line of the flow field, and therefore has double the oscillation frequency. In consistency with the time-averaged flow fields, at the higher Reynolds number there is a clear, although weak, region of fluctuating flow at the middle of the far field, as indicated by the flow patterns in Fig. 6e.

4.2. External jet flow in Lagrangian space

The above analysis revealed that the overall performances of the external flow fields differed considerably between the two Reynolds numbers, which was directly related to the characteristics of the sweeping jet flow. The resulting jet column shape was also found to bend significantly at the higher Reynolds number, resulting in very different flow dynamics of the sweeping jet flow compared with the lower Reynolds number. However, for a jet column with a sweeping motion, detailed analysis of the jet flow is problematic in Eulerian space. Hence, the Lagrangian method was applied instead of using a fixed coordinate. Fig. 7 shows the transformation of a phase-averaged external flow field from Eulerian (red) to Lagrangian (black) space. As shown in Fig. 7a, in the Eulerian system, the jet column maintains an almost straight shape in the near field region ($y < 2d_h$), whereas it bends significantly in the far field region ($y > 4d_h$). In the Lagrangian transformation, the reference frame of the coordinate system (x_j, y_j) is attached on the jet column in the near field region. The origin is set at the center of the jet nozzle, while the x_j -axis and y_j -axis rotate together with the jet column in the near field. The x_j -axis points in the streamwise direction of jet flow, whereas the y_j -axis is normal to it. At this specific instance in Fig. 7, the jet column in the near field region deflects with an angle of θ_L to the center line. In the Lagrangian system, the whole flow field is then rotated back by an angle of $-\theta_L$, as shown in Fig. 7b. To ensure a proper evaluation of θ_L , the coordinate system in Eulerian space is transformed to polar coordinates with polar angles and radial distance r . The origin is fixed at the center of the jet nozzle ($x = 0, y = 0$). Then, the value of θ_L is obtained along an arc with $r/d_h = 2$. As such, the jet columns in the near field region at different phases in Eulerian space are aligned close to the x_j -axis ($y_j = 0$) in Lagrangian space. In addition, as shown in Fig. 7b and 7c, the jet column in the far field generally bends relative to a fixed point on the jet column in the near field. Therefore, an appropriate polar coordinate in

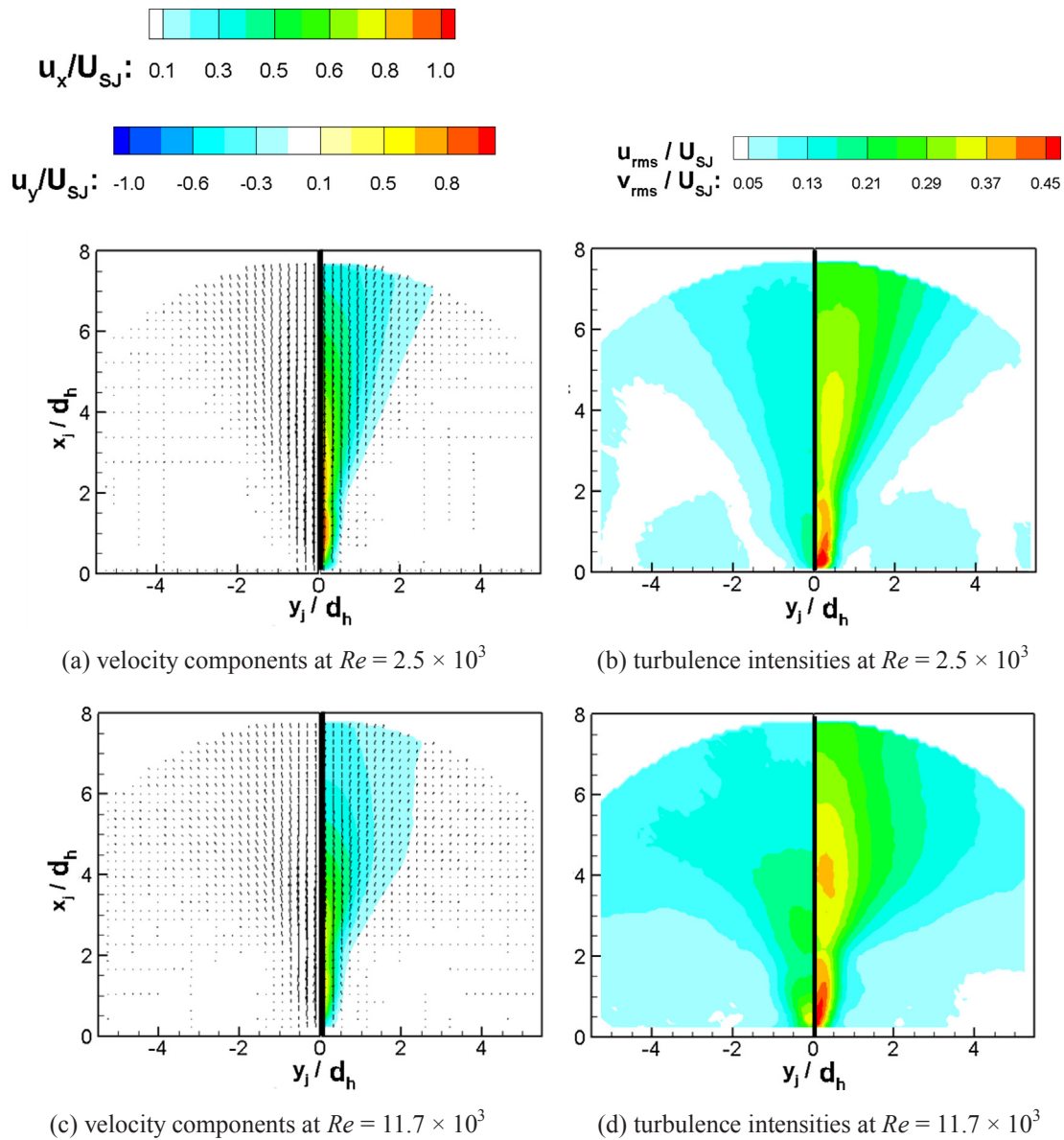


Fig. 8. Time-averaged streamwise velocity along x-direction (right part of the figure) and transverse velocity along y-direction (left side of the figure), and turbulence intensities in streamwise direction (right part of the figure) and transverse direction (left side of the figure), at $Re = 2.5 \times 10^3$ and $Re = 11.7 \times 10^3$ in Lagrangian space. (a) Velocity components at $Re = 2.5 \times 10^3$. (b) Turbulence intensities at $Re = 2.5 \times 10^3$. (c) Velocity components at $Re = 11.7 \times 10^3$. (d) Turbulence intensities at $Re = 11.7 \times 10^3$.

Lagrangian space can be established to extract the jet properties in the far field region. Note that during the transformation, the upper range of Lagrangian space in the streamwise direction is limited to about $x_j/d_h = 8$. This measurement region is large enough to retain the majority of the jet flow during the transformation.

Fig. 8 presents the time-averaged velocity components and turbulence intensities at the two selected Reynolds numbers, i.e. $Re = 2.5 \times 10^3$ and 11.7×10^3 , in Lagrangian space. At the lower Reynolds number, the distributions of the velocity and turbulence intensities are similar to those in Eulerian space due to the small spreading angle of the sweeping jet, as shown in Fig. 8a and 8b. However, the two systems differ significantly at the higher Reynolds number. In Lagrangian space, the velocity components and turbulence intensities are more directed along the center line of the jet flow, as shown in Fig. 8c and d. In the near field region of the jet nozzle at both Reynolds numbers, the width of the jet flow is almost constant. In the far field region, due to the bending of the jet column at the higher Reynolds number, a larger region of high turbulence is induced as

shown in Fig. 8d. Accordingly, the jet velocity decays faster at the higher Reynolds number, as shown in Fig. 8c.

Fig. 9 presents the profiles of streamwise velocity and turbulence intensities along three transverse lines across the jet flow at the two Reynolds numbers. It confirms that in the near field region at $y_i = 1d_h$, the velocity and turbulence profiles are very similar. The streamwise velocity has a peak value at the center of the jet, which is close to the jet velocity U_{Sj} , and then gradually decreases at locations further from the center. Defining the jet width as the normal width of the local velocity profile with $U \geq 50\%U_{max}$, the jet flow has a width of about $1d_h$ at both Reynolds numbers. In contrast, at the far field region at $y_i = 6d_h$, the difference between velocity and turbulence profiles is obvious. The peak value of the streamwise velocity at the higher Reynolds number is only about half of that at the lower Reynolds number, indicating the fast decay of the jet flow momentum. However, the turbulence follows a different trend. Compared with the lower Reynolds number, the turbulence at the higher Reynolds number shows no obvious decay at the far field region. At the outboard region, the turbulence components in

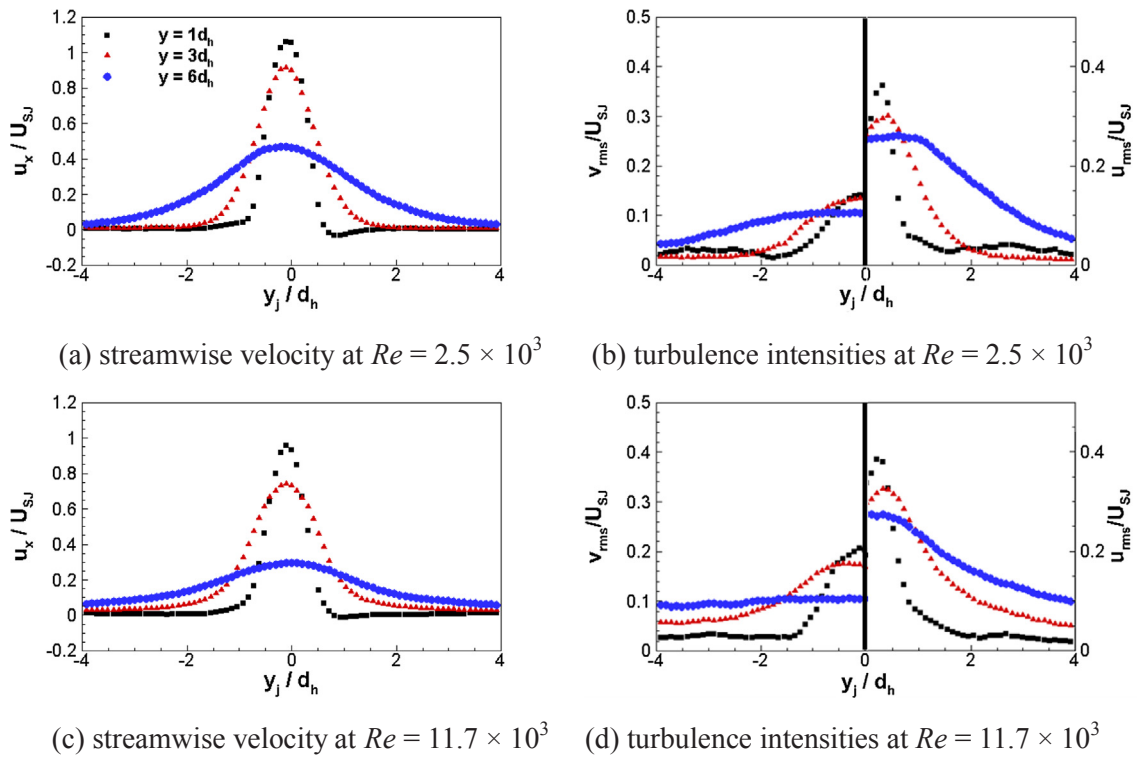


Fig. 9. Time-averaged velocity and turbulence intensity profiles along transverse direction at three streamwise locations at two Reynolds numbers in Lagrangian space. Because the transverse velocity is very small at both Reynolds numbers, its profiles are not shown.

both streamwise and transverse directions are even larger at the higher Reynolds number. This implies that the relatively high fluctuation in the jet flow contributes to the fast decay of the jet velocity in the far field region at this Reynolds number.

To confirm the above results and characterize the jet flows in more detail, phase-dependent profiles of the jet flows at the two Reynolds numbers are plotted for comparison, as shown in Figs. 10 and 11, respectively. Note that because of the jet’s considerable lateral extent in the far field, appropriate comparisons of the jet’s properties at different phases have to be performed at a constant radial distance from a fixed point. Therefore, the coordinate system is transformed to polar coordinates. As shown in Fig. 10a, the fixed point of the polar coordinates is fixed on the jet column in the near field region ($x_j/d_h = 2, y_j = 0$). The jet properties in the far field region are extracted from an arc with a constant distance of $5d_h$ to the fixed point. Fig. 10a to 10d present the time sequences of the phase-averaged jet flow during one half oscillation cycle (the time frame is defined in Eulerian space, as indicated by the dashed lines in Fig. 10f) at the lower Reynolds number. During this half cycle, the jet in the near field region is very stable and stays close to the center line. However, the jet column in the far field sweeps from the left-most side to the right-most side with a small bending angle. The jet properties in the far field region fluctuate only weakly. As shown in Fig. 10e, the jet’s peak velocity and width have mean values of $0.59U_{Sj}$ and $2.2d_h$ with root-mean-squared (RMS) values of 4% and 22%, respectively. By plotting the jet bending angle in the far field (extracted in Lagrangian space) and jet deflection angle in the near field (extracted in Eulerian space) together in Fig. 10f, a clear phase correlation can be seen between the dynamics of the jet flow in the far field and near field regions. For the jet column in the far field, the bending angle to the left side is maximized when the jet in the near field approaches the left side at $t/T = 0.3$. After that, as the jet in the near field region arrives and stays at the left-most position, the jet bending angle in the far field decreases, indicating a return to the straight jet shape (as also shown in Fig. 10b and 10c by the phase-averaged flow at $t/T = 0.46$ and 0.63). When the jet sweeps back to the left side in the near field, the jet’s

bending angle to the right in the far field is maximized, as shown in Fig. 10d at $t/T = 0.8$. Therefore, the phase difference between the dynamics of the jet flow in the near field and far field regions is found to be about $0.7T$. In addition, it is found that the maximum jet bending angle in the far field is similar to the maximum jet spreading angle in the near field, i.e. about 20° .

At the higher Reynolds number, larger bending angles of the jet column in the far field region are generated, as shown by the phase-averaged jet flow fields in Fig. 11a to d. The large bending angles also lead to high fluctuations of the jet properties in the far field. As shown in Fig. 11e, the jet peak’s mean velocity of $0.4U_{Sj}$ is smaller at this Reynolds number due to the larger mean jet width of $3d_h$. The RMS fluctuations of velocity and width are about 10% and 90%, respectively, which are much higher than those at the lower Reynolds number. In addition, there is a clear correlation between the fluctuating trends of the peak jet velocity and the jet width. One value wanes while the other waxes. The minimum peak jet velocity is found when the jet is maximally bent, whereas the jet width is almost maximized at this point, although there is a slight phase shift. Fig. 11f shows that the jet column has a bending angle of about 50° in the far field region, which is even larger than the spreading angle in the near field region. In addition, the oscillation patterns of the jet bending angle in the far field are more uneven than those in the near field region. The jet bends and recovers more quickly, resulting in obvious plateau periods with only small bending angles at the time periods of about $0 < t/T < 0.15$ and $0.5 < t/T < 0.65$. The highly fluctuating jet properties and uneven jet oscillation patterns also explain the weak flow in the middle of the far field region in Eulerian space (as demonstrated in Fig. 7a and b). In Eulerian space, due to the bending of the jet column in the far field, the jet momentum is distributed in the middle of this region only when the jet in the near field region reaches the maximum deflection. The Lagrangian analysis shows that the jet column recovers rapidly from the bent shape. Therefore, in Eulerian space, only a limited time window is available to distribute the jet momentum in the middle of the far field region. In addition, the jet velocity in the far field region is significantly

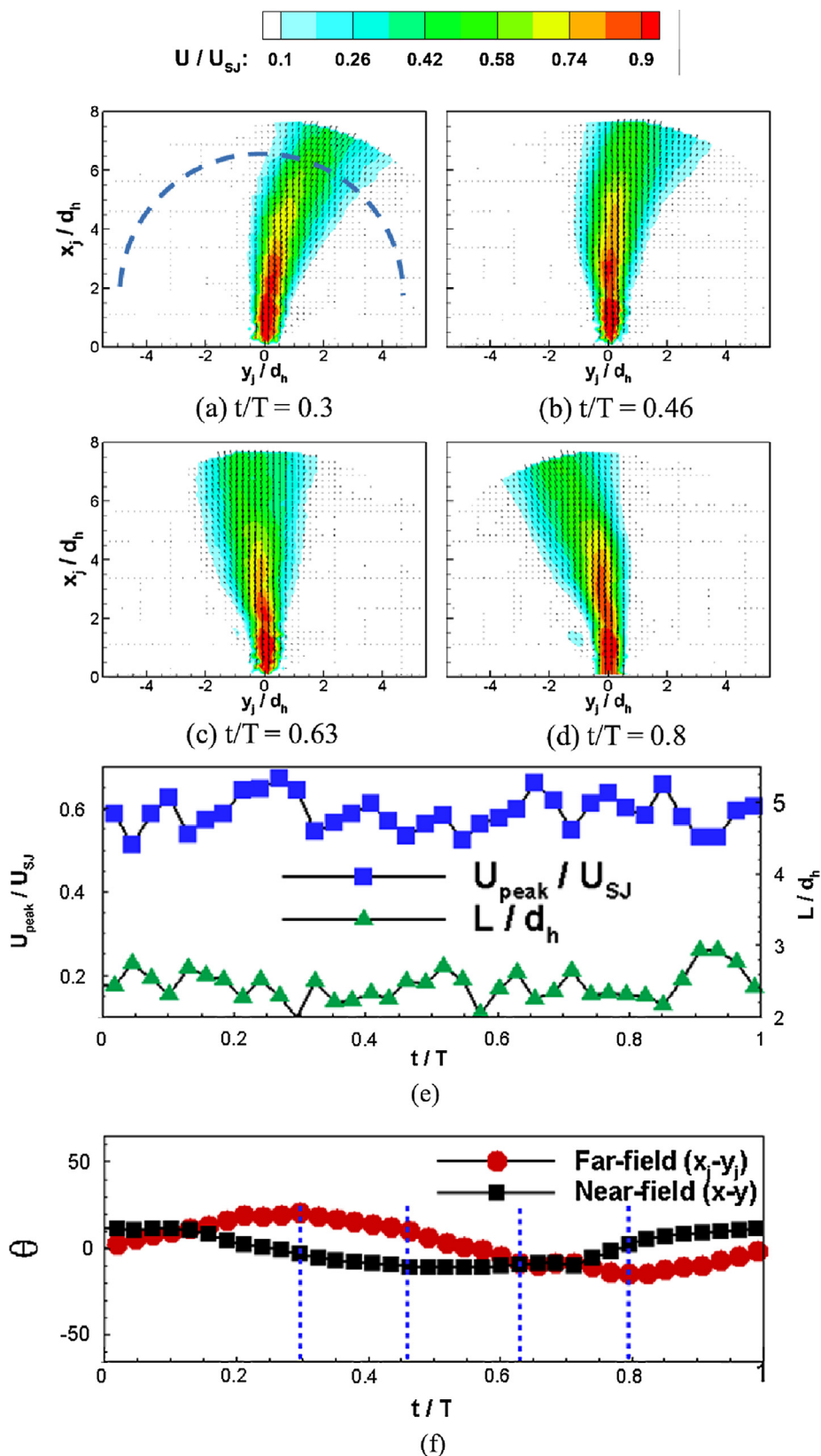


Fig. 10. (a–d) Contour of phase-averaged velocity magnitude during half sweeping cycle in Lagrangian space, (e) oscillation patterns of jet peak velocity U_{peak} and jet width L in the far field and (f) jet bending angle in the far field (Lagrangian space) and jet deflection angle in the near field (Eulerian space) at $Re = 2.5 \times 10^3$. The uncertainties of the peak velocity and jet width are about 2% and 5% relative to the mean values, respectively.

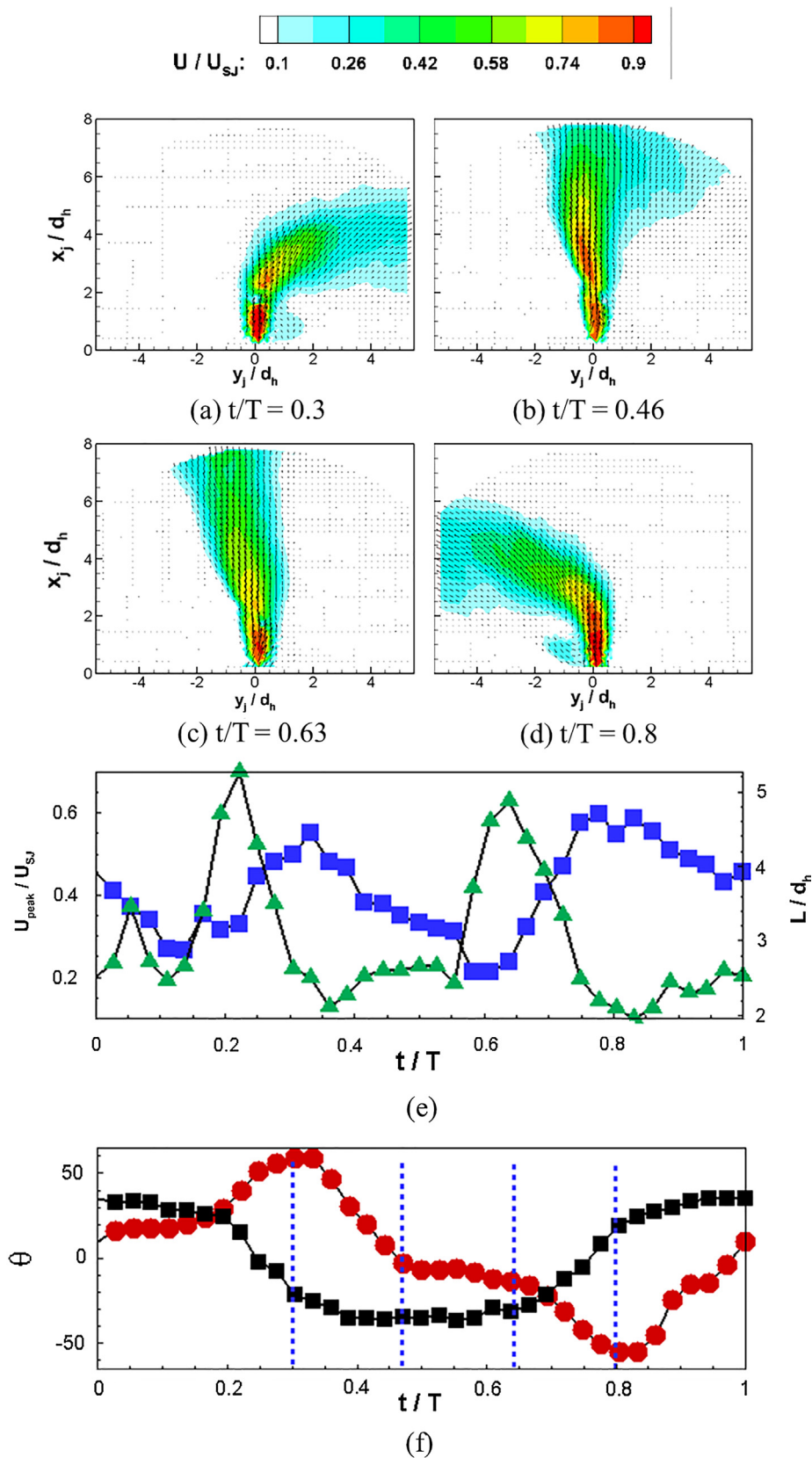


Fig. 11. (a–d) Contour of phase-averaged velocity magnitude during half sweeping cycle in Lagrangian space, (e) oscillation patterns of jet peak velocity U_{peak} and jet width L in the far field and (f) jet bending angle in the far field (Lagrangian space) and jet deflection angle in the near field (Eulerian space) at $Re = 11.7 \times 10^3$. The uncertainties of the peak velocity and jet width are about 2% and 3% relative to the mean values, respectively.

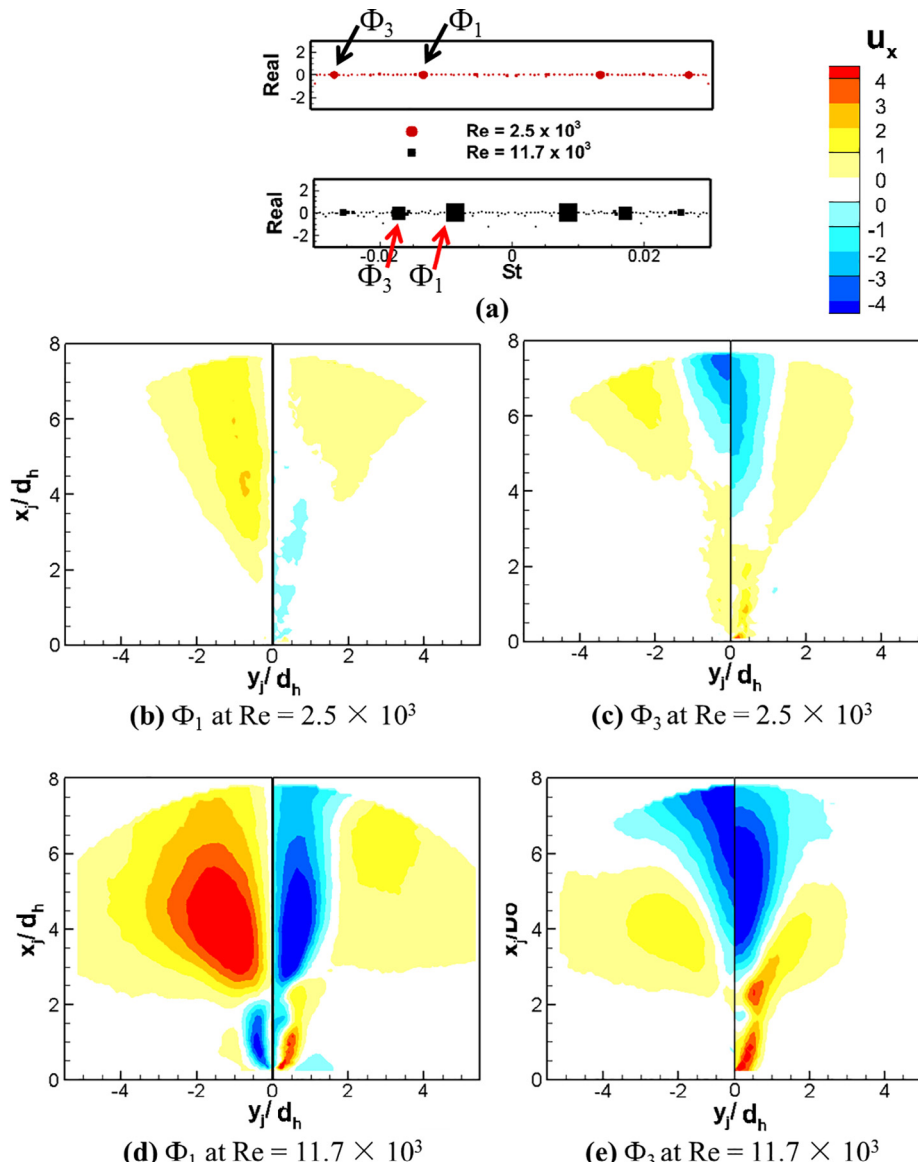


Fig. 12. (a) Energy and frequency spectra of DMD modes (size of the solid symbols indicates the captured energy of each mode), (b–e) contour of streamwise velocity captured by the first two mode-pairs (real part on the left of the figure and imaginary part on the right), in Lagrangian space.

dissipated when the jet column is bent. These characteristics of the jet flow result in the weak flow in the middle of the far field region in Eulerian space. Despite the different flow dynamics, one interesting common feature between the two Reynolds numbers is that the phase correlations between the jet bending angle in the far field and jet deflection angle in the near field are very similar, both having a phase difference of about 0.7π , as shown in Fig. 11f.

Unlike in Eulerian space, Lagrangian DMD analysis can capture the variation of the jet flow, especially the flow dynamics in the far field region. The energy levels of the fluctuating modes are much lower than those in Eulerian space, as shown by the symbol sizes in Fig. 12a. This is to be expected, because the Lagrangian transformation eliminates the spatial variation of the near field jet dynamics. Therefore, Lagrangian DMD accurately captures the fluctuating flow patterns induced by the bending jet column in the far field region. The DMD modes reveal that the fluctuating flow patterns are similar at both Reynolds numbers. As shown in Fig. 12b to 12e, the first mode-pair captures the flow patterns at the bilateral sides of the jet center line in the far field region, whereas the second mode-pair mostly captures the flow patterns along the jet center line. Similar to those in Eulerian space, the frequency of the first

mode-pair is the oscillation frequency, whereas that of the second is double this frequency, as shown in Fig. 12a. However, there are still some differences between the two Reynolds numbers. The fluctuating patterns are much stronger at the higher Reynolds number, as indicated by the higher energy levels and the larger size of the flow patterns. This is induced by the larger bending angle of the jet column and the highly fluctuating velocity in the far field, as shown previously.

5. Conclusions

In this study, the flow dynamics of a sweeping jet generated by a fluidic oscillator at six Reynolds numbers is experimentally investigated by TR-PIV. With the increase of Reynolds number from $Re = 2.5 \times 10^3$ to 11.7×10^3 , the spreading angle of the external jet increases, and reaches its saturation value at $Re = 10 \times 10^3$. The normalized oscillation frequency St shows a clear declining trend with the increase of Reynolds number. Inside the oscillator, two bilateral separation bubbles are generated between the main jet and the side walls of the mixing chamber. The size of the separation bubbles increases with the Reynolds number, resulting in a larger spreading angle of the external

jet flow and a lower oscillation frequency. Particular attention is paid to the external jet flow behaviors at two Reynolds numbers, $Re = 2.5 \times 10^3$ and 11.7×10^3 , which respectively correspond to the occurrences of straight and deflected jet columns.

The external flow fields show that the distributions of the jet momentum differ between the two Reynolds numbers, as revealed in Eulerian space. The time-averaged flow momentum is more evenly distributed at the lower Reynolds number, whereas it is more directed toward the maximum deflected positions of the jet at the higher Reynolds number. DMD analysis reveals that the major fluctuating flow patterns behave similarly to the flow momentum, resulting in a clear weak-flow region at the middle of the far field region from the jet nozzle at the higher Reynolds number. The resulting jet column shape is also found to bend significantly, being highly curved at the higher Reynolds number.

By attaching a rotating reference frame on the jet column, a Lagrangian transformation is applied to enable the appropriate comparison of the jet flows with different column shapes. The large bending angle introduces greater fluctuation and more uneven oscillation patterns in the far field region at the higher Reynolds number. The time-averaged velocity and turbulence intensities show that the jet flows at the two Reynolds numbers are similar in the near field region. However, in the far field region, the jet velocity decreases faster, with higher turbulence intensities, at the higher Reynolds number. The phase-dependent jet flows confirm that the peak velocity and the jet width fluctuate at least twice as strongly during the oscillation cycle at the higher than at the lower Reynolds number. The larger jet bending angle in the far field region also shows more uneven oscillation patterns compared with those in the near field region. These highly fluctuating and uneven flow oscillations also contribute to the weak flow in the far field region in Eulerian space. In addition, spatially larger and more strongly fluctuating patterns in the far field of the jet flow are clearly induced by the large bending angle of the jet column, as captured by Lagrangian DMD.

Conflict of interest

The authors declare that we do not have any commercial or associative interest that represents a conflict of interest in connection with the work submitted.

Acknowledgments

The authors gratefully acknowledge the financial support from the National Natural Science Foundation of China (Grant nos. 11702172 and 11725209) for this study.

References

- [1] L. Agricola, M.A. Hossain, R. Prenter, R. Lundgreen, A. Ameri, J. Gregory, J.P. Bons, Impinging sweeping jet heat transfer, *AIAA Paper* (2017) 2017–4974.
- [2] B.C. Bobusch, R. Wozidlo, J.M. Bergada, C.N.N. Nayeri, C.O. Paschereit, Experimental study of the internal flow structures inside a fluidic oscillator, *Exp. Fluids* 54 (6) (2013) 1559.
- [3] B. Cabral, L.C. Leedom, Imaging vector fields using line integral convolution, *ACM* 27 (1993) 263–270.
- [4] S. Gaertlein, R. Wozidlo, F. Ostermann, C.N. Nayeri, C.O. Paschereit, The time-resolved internal and external flow field properties of a fluidic oscillator, *AIAA Paper* (2014), <http://dx.doi.org/10.2514/6.2014-1143>.
- [5] M. Koklu, Effect of a Coanda extension on the performance of a sweeping-jet actuator, *AIAA J.* 54 (3) (2016) 1–4.
- [6] R.K. Lundgreen, A.F. Hossain, R. Prenter, J.P. Bons, J.W. Gregory, A. Ameri, Impingement heat transfer characteristic of a sweeping jet, *AIAA paper*, Aerospace Sciences Meeting, 2017, 2017-1535.
- [7] F. Ostermann, R. Wozidlo, C.N. Nayeri, C.O. Paschereit, Experimental comparison between the flow field of two common fluidic oscillator designs, *AIAA paper*, Aerospace Sciences Meeting, 2015a, 2015-0781.
- [8] F. Ostermann, R. Wozidlo, S. Gaertlein, C.N. Nayeri, C.O. Paschereit, Phase-averaging methods for the natural flow field of a fluidic oscillator, *AIAA J.* 53 (8) (2015) 2359–2368.
- [9] M. Raffel, C.E. Willert, J. Kompenhans, *Particle Image Velocimetry: A Practical Guide*, Springer, Berlin, 2013.
- [10] P.J. Schmid, Dynamic mode decomposition of numerical and experimental data, *J. Fluid Mech.* 656 (10) (2010) 5–28.
- [11] P.J. Schmid, Application of the dynamic mode decomposition to experimental data, *Exp. Fluids* 50 (4) (2011) 1123–1130.
- [12] R. Seele, P. Tewes, R. Wozidlo, M.A. McVeigh, N.J. Lucas, I.J. Wygnanski, Discrete sweeping jets as tools for improving the performance of the V-22, *J. Aircraft* 46 (6) (2009) 2098–2106.
- [13] J. Sesterhenn, A. Shahirpour, A Lagrangian dynamic mode decomposition, 2016, arXiv:1603.02539.
- [14] A.S. Sharma, I. Mezić, B.J. McKeon, Correspondence between Koopman mode decomposition, resolvent mode decomposition, and invariant solutions of the Navier-Stokes equations, *Phys. Rev. Fluids* 1 (3) (2016) 032402(R).
- [15] X. Wen, Y. Liu, H. Tang, Unsteady behavior of a sweeping impinging jet: Time-resolved particle image velocimetry measurements, *Exp. Therm Fluid Sci.* (2018), <http://dx.doi.org/10.1016/j.exptthermfluidsci.2018.02.033>.
- [16] C.E. Willert, M. Gharib, Digital particle image velocimetry, *Exp. Fluids* 10 (4) (1991) 181–193.
- [17] R. Wozidlo, F. Ostermann, C.N. Nayeri, C.O. Paschereit, The time-resolved natural flow field of a fluidic oscillator, *Exp. Fluids* 56 (6) (2015) 125.
- [18] S. Yasuhiko, N. Shigeru, O. Taketoshi, O. Koji, A highly accurate iterative PIV technique using a gradient method, *Meas. Sci. Technol.* 11 (12) (2000) 1666.